

A Universal Wideband Device-Level Parallel Simulation Method and Conducted EMI Analysis for More Electric Aircraft Microgrid

Ruimin Zhu¹, Student Member, IEEE, Zhen Huang², Student Member, IEEE,
and Venkata Dinavahi², Fellow, IEEE

Abstract—The validation of electromagnetic compatibility for the microgrid of a more electric aircraft (MEA) is an essential test item before delivery for a trial flight, and it has always been urgently expected to be involved during the design stage. This article presents a universal method for wideband modeling and simulation of the MEA microgrid system in the time domain, regardless of the fact that motors are driven by which kind of converter, e.g., modular multilevel converter (MMC), 3-L neutral-point clamped (NPC), or 2-L pulsewidth modulation (PWM) converters. The insulated gate bipolar transistor and diodes are modeled with the physics-based dynamic model to emulate not only precise system-level performance of the system, but also to get an insight into the high-frequency oscillation between junction capacitance of the semiconductor modules and the parasitic parameters and high-frequency branch of other components, such as the permanent magnet synchronous motor (PMSM), transformer, and generator. To alleviate the attendant computational challenge, which could be extremely time-consuming (if no nonconvergence problem is encountered) when solved on traditional simulation platform, circuit partition based on transmission line decoupling, Norton equivalent parameter extraction, and TLM-link decoupling of submodules from the MMC bridge arms are utilized. The simulation program is executed on GPU to achieve massively parallel and accelerated solution. The accuracy and efficiency of the GPU-based parallel algorithm are validated by the comparison with the experimentally verified model in ANSYS Simplorer.

Index Terms—Electromagnetic interference (EMI), graphics processor, insulated gate bipolar transistor (IGBT), massively parallel processing, modular multilevel converter (MMC), more electric aircraft (MEA), wideband modeling.

I. INTRODUCTION

THE groundbreaking more electric aircraft (MEA) technology has received tremendous attention in recent years

Manuscript received January 1, 2020; revised May 5, 2020 and May 25, 2020; accepted June 13, 2020. Date of publication June 18, 2020; date of current version October 21, 2020. This work was supported by the Natural Science and Engineering Research Council of Canada (NSERC). (Corresponding author: Zhen Huang.)

Ruimin Zhu is with the School of Electrical and Electronic Engineering, North China Electric Power University, Baoding 071003, China, and also with the Department of Electrical and Computer Engineering, University of Alberta, Edmonton, AB T6G 1H9, Canada (e-mail: zruimin@ualberta.ca).

Zhen Huang and Venkata Dinavahi are with the Department of Electrical and Computer Engineering, University of Alberta, Edmonton, AB T6G 1H9, Canada (e-mail: zh2@ualberta.ca; dinavahi@ualberta.ca).

Color versions of one or more of the figures in this article are available online at <https://ieeexplore.ieee.org>.

Digital Object Identifier 10.1109/JESTIE.2020.3003317

for its exceptional advantage, such as enabling higher fuel efficiency, bringing quieter flight experience, and reducing maintenance costs [1], [2]. Some industry-leading aircraft, e.g., Boeing 787 and Airbus A380, have replaced traditional hydraulic, mechanical, or pneumatic power sources for the corresponding load with electric power. The adoption of more electric concept obviously puts a significantly larger load on the electrical system and more demand on power electronic converters with semiconductor devices onboard, which will inevitably introduce electromagnetic interference (EMI) due to the high dv/dt and di/dt slew rate.

Absolutely, safety issues should be treated with the utmost seriousness during aircraft design and operation. The National Aeronautics and Space Administration (NASA) has provided an investigation into the history of some EMI-related malfunction in the military and commercial aerospace program [3]. In terms of EMI, even the availability of a wireless network in the passenger cabin needs critical test and cautious validation [4]. In conjunction with the failures and anomalies, the radiated electromagnetic disturbance noise may cause on the electronic systems installed onboard for flight navigation communication and control, even motor premature winding failure, ball-bearing deterioration, and motor terminal overvoltages [5] could be brought about by the common mode conducted EMI from the driving converter. Thus, it is favorable if the prediction for the conducted EMI, which is the prerequisite of radiated noise precaution and the shield configuration as well as the passive filter's installation guidance, could be conducted closely after the completion of the design blueprint and before the prototype manufacturing stage.

The accurate prediction of EMI, which implicates both the transient switching action of the semiconductor devices and parasitic parameter extraction of the equipment, is undoubtedly the first step and foundation for the validation and presupposition to propose reasonable attenuation strategy. System-level or behavior layer performance has been examined with the insight into transient response and control strategy optimization [6]–[8]. However, the modeling of the semiconductor devices as a two-state ideal switch or piecewise linear behavior model cannot enable the revealing of the high-frequency characteristics. Detailed physics-based models of the switches are rarely included in large-scale power converters simulation for the obstacle due to their nonlinear characteristics [9] and long simulation time.

Alternatively, graphic-fitting-based methods [10], [11] are used for the estimation of the EMI level, in which the switching waveforms are approximated as simplified shapes, such as trapezoidal, S-shaped, or sinusoidal. Consequently, the precision issues may come from this compromise and, furthermore, the impact from the control system fails to be included and the EMI characteristics cannot be analyzed comprehensively under varying operation modes of the aircraft.

To avoid the complex modeling and simulation of the large-scale power converter in the time domain [12]–[15], measurement-based methods in the frequency domain were proposed to characterize a given prototype with the equivalent source and impedance network via a specific test procedure [16]–[18] under a certain operating condition. Nevertheless, the dependence on measurement makes it unachievable for EMI verification before the system is constructed, which essentially should be classified more like a step within the trial and error process rather than a prediction method. As a matter of fact, experimental determination for the EMC validation for the aircraft of various types could be particularly uneconomical and impractical.

Thus, it is imperative to perform device-level time-domain simulation, which can not only gain adequate insight into system-level emulation, power loss estimation for the numerous onboard converters, and well coordination for the control strategy, but also the preliminary test of EMC, thereby achieving an overall optimization and coordination of the whole MEA microgrid system during the early design stage, enabling more efficient planning for potential equipment failure or anomaly.

All the aforementioned facts come to the conclusion that the simulation of a complex system with a physics-based model of semiconductor devices, stray parameters of the converters, and wideband model of other equipment could be extremely hard but urgently needed, which poses a challenge to existing simulation platform such as Simulink and PSCAD/EMTDC. In this article, the wideband model of the overall MEA microgrid is simulated via a highly efficient parallel method based on circuit partitioning. The GPU's massive parallelism is utilized to expedite the simulation of wideband device-level converters.

The article is organized as follows. Section II shows the overall system construction of the considered MEA microgrid and the component level decoupling method. Section III presents the nonlinear advanced dynamic insulated gate bipolar transistor (IGBT)/diode electro-thermal model and the wideband model of the 2-L pulsewidth modulation (PWM) converter, 3-L neutral-point clamped (NPC) converter, and modular multilevel converter (MMC). Section IV shows the detailed partitioning methodologies of the GPU-accelerated simulation framework and overall impact analysis of different factors. Finally, Section V concludes this article.

II. MORE ELECTRIC AIRCRAFT MICROGRID SYSTEM

A. More Electric Architecture of Boeing 787 Aircraft

Fig. 1 shows the whole more electric architecture of Boeing 787 aircraft. Along with the propulsion thrust for the flight, all the onboard loads are supplied by six gas turbine engines, of

which four main generators (250 kVA) are distributed on both wing sides, and the other 2×225 kVA auxiliary power unit are installed at the tail end of the aircraft. All these synchronous generators are operated in a “bleedless” manner, which means that the pneumatic power extraction in the traditional engine technology is removed and connected to the electrical power distribution system to achieve the resilient operation with minimum redundancy [19]. The generator is driven directly by a shaft in the gas turbine, thus, providing a variable-frequency 230 V ac supply from 360 to 800 Hz. Besides, a pre-emergency ram air turbine is used to provide electric power under crisis conditions [20].

The wing ice protection system, which is actually an embedded resistive heat load, is directly connected to the ac bus. The permanent magnet synchronous motor (PMSM) loads for the environmental control system are supplied through the autotransformer rectifier unit (ATRU) using 270 V dc bus, whose detail is given in Fig. 1(b) and (c). The electromechanical actuators are connected onto the ac bus via a dc–dc converter to enable flight-critical control and aircraft braking and fuel pumping. An extra 28 V dc bus is added to provide battery charge power through the transformer rectifier unit (TRU).

B. Microgrid System Decoupling

1) *Wideband Model of Cable*: The subsystems of the microgrid are connected with dc and ac cables, as shown in Fig. 2, whose wideband characteristics include the frequency-dependent parameter variation of series impedance and shunt admittance per unit length matrix, which should be taken into account during the EMI analysis. Thus, the frequency-dependent line model (FDLM) [21] is utilized to present the corresponding high-frequency characteristics and furthermore provide the subsystem partitioning.

The terminal current equations in the frequency domain for a transmission line of length l are expressed as

$$I_A = Y_C \cdot V_A - 2I_{Ai} = Y_C \cdot V_A - 2HI_{Br} \quad (1)$$

$$I_B = Y_C \cdot V_B - 2I_{Bi} = Y_C \cdot V_B - 2HI_{Ar} \quad (2)$$

where $Y_C = \sqrt{Y/Z}$ represents the characteristic admittance matrix, and $H = e^{(-\gamma x)}$ and $\gamma = \sqrt{ZY}$ represent the propagation matrix and constant, respectively. I_{Ai} and I_{Bi} are the incident currents, whereas I_{Ar} and I_{Br} are the reflected currents, as shown in Fig. 2(b). The corresponding time-domain equations are formulated as

$$i_A(t) = y_c * v_A(t) - 2h * i_{Br}(t) \quad (3)$$

$$i_B(t) = y_c * v_B(t) - 2h * i_{Ar}(t). \quad (4)$$

By applying vector fitting techniques, Y_C and H can be approximated as

$$Y_C(i, j) = \sum_{m=1}^{N_p} \frac{r_{Y_C(i, j)}(m)}{s - p_{Y_C}(m)} + d(i, j) \quad (5)$$

$$H(i, j) = \sum_{k=1}^{N_g} \sum_{n=1}^{N_{p, k}} \frac{r_{H(i, j), k}(n)}{s - p_{H, k}(n)} e^{-s\tau_k}. \quad (6)$$

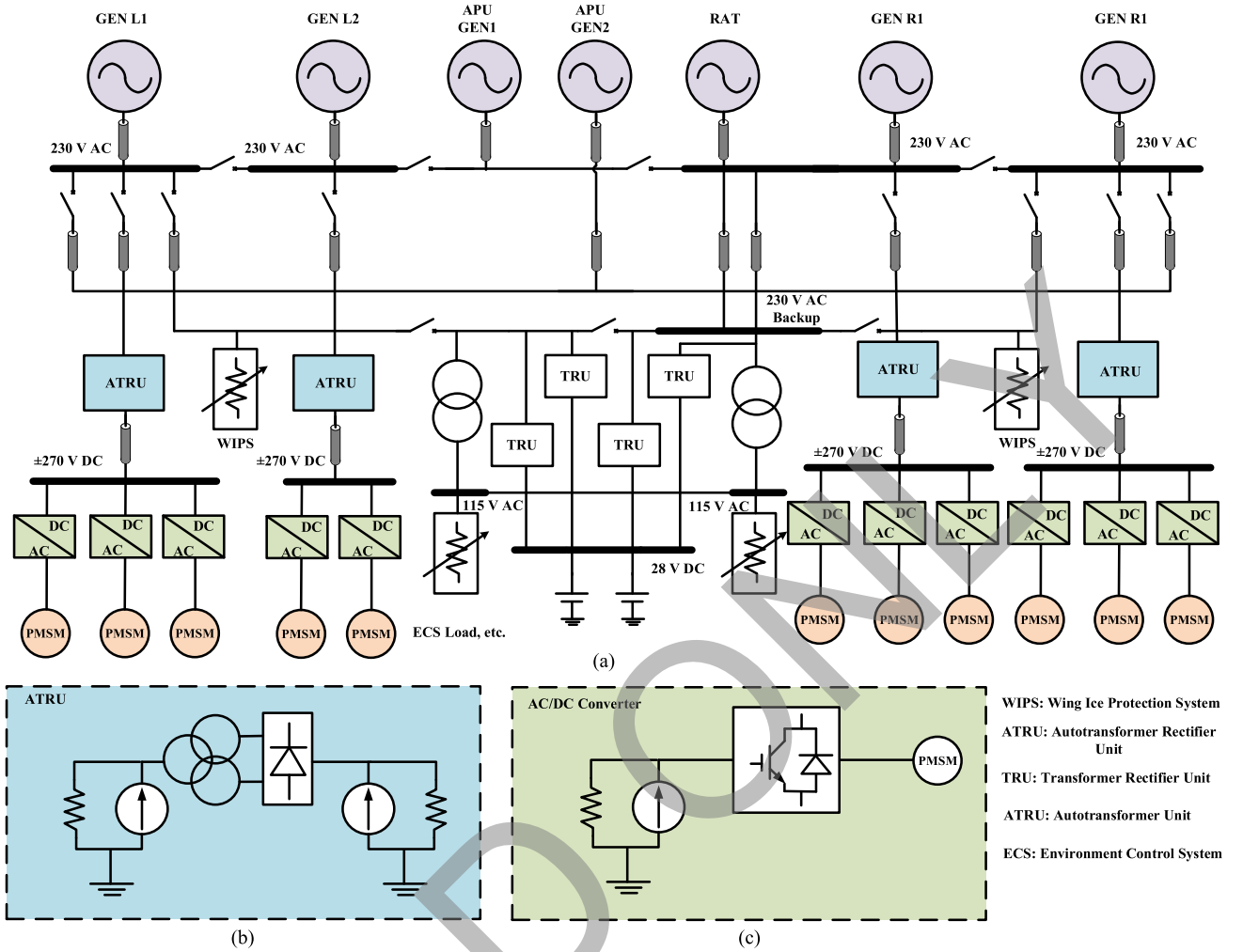


Fig. 1. Micro grid of Boeing 787 aircraft. (a) Overall system. (b) Decoupled subcircuit of the ATRU. (c) Decoupled subcircuit of the converter.

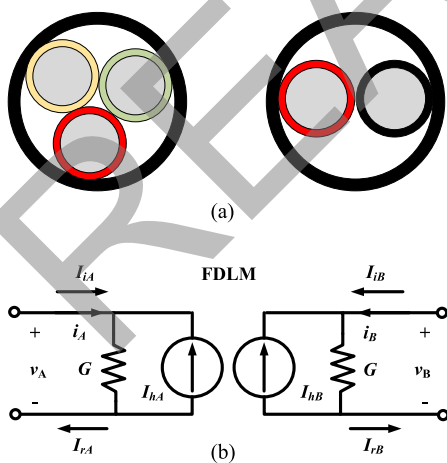


Fig. 2. FDLM of ac and dc cable. (a) AC and dc cable. (b) Decoupled cable model.

Thus, the $g(t) = y_c * v_A(t)$ convolution can be calculated recursively by introducing a state variable vector $x^{(i)}(t)$ and applying Trapezoid Rule and followed with the variable composition

$x^{*(i)}(n) = x^{(i)}(n) - \lambda_{Y_C}^{(i)}(n)v_A(n)$. The discretized state-space equations are

$$x^{*(i)}(n) = \alpha_{Y_C}^{(i)}(n)x^{*(i)}(n-1) + (\alpha_{Y_C}^{(i)}(n)\lambda_{Y_C}^{(i)}(n-1) + \mu_{Y_C}^{(i)}(n))v_A(n-1) \quad (7)$$

$$g(n) = \sum_{i=1}^{N_p} r_{Y_C}^{(i)}x^{(i)}(n) + G_A(n)v_A(n). \quad (8)$$

where

$$\alpha_{Y_C}^{(i)} = \left(1 + p_{Y_C}^{(i)} \frac{\Delta t_n}{2}\right) / \left(1 - p_{Y_C}^{(i)} \frac{\Delta t_n}{2}\right) \quad (9)$$

$$\lambda_{Y_C}^{(i)} = \mu_{Y_C}^{(i)} = \left(\frac{\Delta t_n}{2}\right) / \left(1 - p_{Y_C}^{(i)} \frac{\Delta t_n}{2}\right). \quad (10)$$

The two terminals of the cable are decoupled in topology while maintaining their electrical interaction, as shown in the Fig. 2(b), and the parameters of the line model are listed in Tables I and II of Appendix.

2) *Wideband Model of Transformer and PMSM*: As shown in Fig. 3, one phase of the wideband transformer model takes

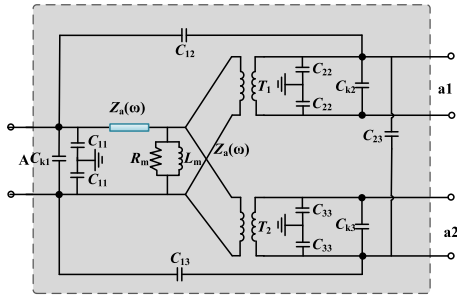


Fig. 3. Wideband model of one phase of transformer.

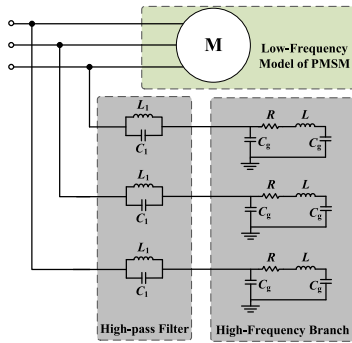


Fig. 4. Wideband model of PMSM.

skin effect, proximity effect, and stray capacitances intersecting among terminals, which are frequency-dependent, into consideration. The two ports of the three phase at the secondary side are connected in the star and delta form, respectively. The nonlinear characteristics of the iron core are neglected for the skin effect under high frequencies. The magnetizing impedance is modeled as a resistance R_m paralleled with an inductance L_m . The leakage impedance is modeled by an R - L ladder network, with the parameters characterization process elaborated in [25]. The interterminal capacitances reflect the stray effects, which will exert more significant impact on the circuit. T1 and T2 are ideal transformers with the rated voltage ratio.

Fig. 4 shows the wideband motor model utilized in this article [24]. The lumped high-frequency branch is obtained through a reduced-order process, which employs the Kron reduction method. The parallel connection enables insight into the wideband characteristics and the dynamics at low frequencies, which will facilitate the time-domain simulation under various work conditions. The parameters of the PMSM model are listed in Table III of Appendix.

3) *System Level Decoupling*: Undoubtedly, the whole microgrid of the MEA is a system with considerable scale and numerous nodes, for which the model established and solved in Simplorer or Saber will be extremely time-consuming. When the dimension comes to a specific level, the coefficient matrix in the system equation will be significantly large so that the entire system simulation will be hard to converge. However, in this article, the calculation burden is alleviated by a hierarchical circuit partitioning architecture based on the FDLM and

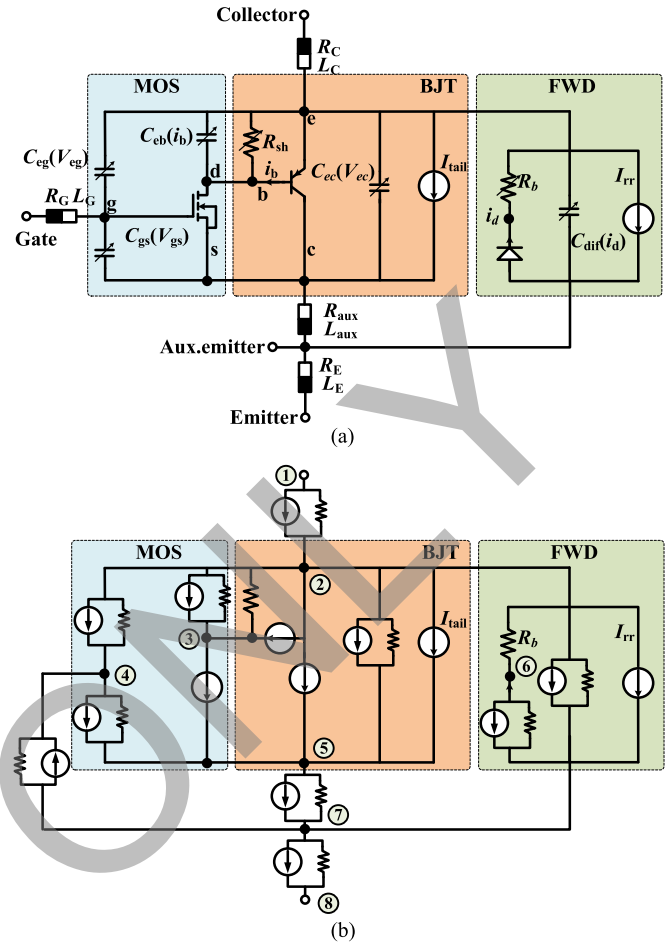


Fig. 5. Model details of IGBT and FWD. (a) Schematic of dynamic IGBT model. (b) Discretized model.

semiconductor devices equivalent subcircuits extraction of each converter to split the whole system into several smaller blocks with the reduced matrix size. The generator, PMSM, and ATRU units are all decoupled from the system with one equivalent end circuit of the FDLM connected to the corresponding terminal. Therefore, no matter how large the system is, the scale of the subcircuits will be fixed. Furthermore, if each of them was solved in a parallel architecture, no significant increase will be faced in the simulation time.

III. DEVICE PARTITIONING FOR PARALLEL SIMULATION

A. IGBT/Diode Electro-Thermal Model

A physics-based dynamic model of IGBT and diode [23] is employed to present the static and transient switching characteristics. As shown in Fig. 5(a), the equivalent circuit of the IGBT module contains eight nodes from three parts representing a metal oxide semiconductor (MOS) structure, bipolar junction transistor (BJT) component, and the freewheeling diode chip. The main framework determines the static working point of the IGBT is a Darlington combination of MOSFET and BJT.

The output characteristics of the cutoff, linear, and saturation regions of the MOSFET part is described by

$$I_{\text{mos}} = \begin{cases} 0, & V_{gs} < V_P \\ I_{\text{sat}} \cdot (1 + K_{LM} \cdot V_{ds}), & V_{gs} < V_P \\ (2 - \frac{V_{ds}}{V_{\text{sat}}}) \cdot \frac{V_{ds}}{V_{\text{sat}}}, & V_{ds} < V_{\text{sat}} \\ I_{\text{sat}} \cdot (1 + K_{LM} \cdot V_{ds}), & V_{ds} \geq V_{\text{sat}} \end{cases} \quad (11)$$

where V_{ds} and V_{gs} are the voltage across the corresponding nodes, V_P is the threshold voltage of the channel, and V_{sat} and I_{sat} are saturation voltage and current formulated as

$$V_{\text{sat}} = A_{\text{FET}} (V_{gs} - V_P)^{M_{\text{FET}}} \quad (12)$$

$$I_{\text{sat}} = \frac{K}{2} (V_{gs} - V_P)^{N_{\text{FET}}} \quad (13)$$

where A_{FET} , M_{FET} , N_{FET} , K , and K_{LM} are all model coefficients. As regard to the BJT, the forward conduction state of the $P^+ - N^-$ junction is considered as a diode described as

$$I_b = I_{\text{SAT}_{\text{BJT}}} \cdot \left[e^{\frac{V_{eb}}{(M_{\text{BJT}} \cdot V_T)}} - 1 \right] \quad (14)$$

where V_{eb} and I_b are the base-emitter voltage and base current. $I_c = b_n \cdot I_b$ is the collector current, $V_T = \frac{kT}{q}$ is the thermal voltage, and $I_{\text{SAT}_{\text{BJT}}}$, M_{BJT} , and b_n are the coefficients to be extracted.

There are several nonlinear capacitances in the model to emulate the switching characteristics, which can be classified into two categories: capacitance for the PN junction and the diffusion region in the ON-state. The corresponding capacitances are given as

$$C(V_{\text{JVCT}}^*) = \begin{cases} C_0 \cdot (1 + (\beta - 1)(1 - \exp(-\frac{\alpha(1-\delta)V_{\text{JVCT}}^*}{(\beta-1)V_{\text{diff}}}))), & V_{\text{JVCT}}^* > 0 \\ C_0 \cdot \left(\delta + \frac{1-\delta}{(1 - \frac{V_{\text{JVCT}}^*}{V_{\text{diff}}})^\alpha} \right), & V_{\text{JVCT}}^* \leq 0 \end{cases} \quad (15)$$

where C_0 , α , β , δ , and V_{diff} are all coefficients, which have their corresponding value for each junction capacitance; V_{JVCT}^* is expressed as

$$V_{\text{JVCT}}^* = K_{\text{shift}} \cdot V_{\text{diff}} - V_{\text{JNCT}} \quad (16)$$

where K_{shift} is the coefficient, and V_{JNCT} is the junction voltage.

The diffusion capacitances for the BJT and FWD components are modeled as

$$C_{\text{diff}} = \tau \frac{i(t) + I_{\text{SAT}}}{M \cdot V_T} \quad (17)$$

The FWD is modeled as a combination of a nonlinear diode in series with a current-dependent resistance:

$$I_{\text{fwd}} = I_{\text{SAT}_{\text{fwd}}} \cdot \left[e^{\frac{V_{\text{fwd}}}{(M_{\text{fwd}} \cdot V_T)}} - 1 \right] \quad (18)$$

$$R_b = \frac{Rb_{\text{fwd}}}{\sqrt{1 + \frac{I_{\text{fwd}}}{I_{\text{NOM}}}}} \quad (19)$$

where $I_{\text{SAT}_{\text{fwd}}}$, M_{fwd} , and Rb_{fwd} are all the coefficients, and I_{NOM} is the rated current. The waveform of reverse recovery current and the tail current is elaborated in [23].

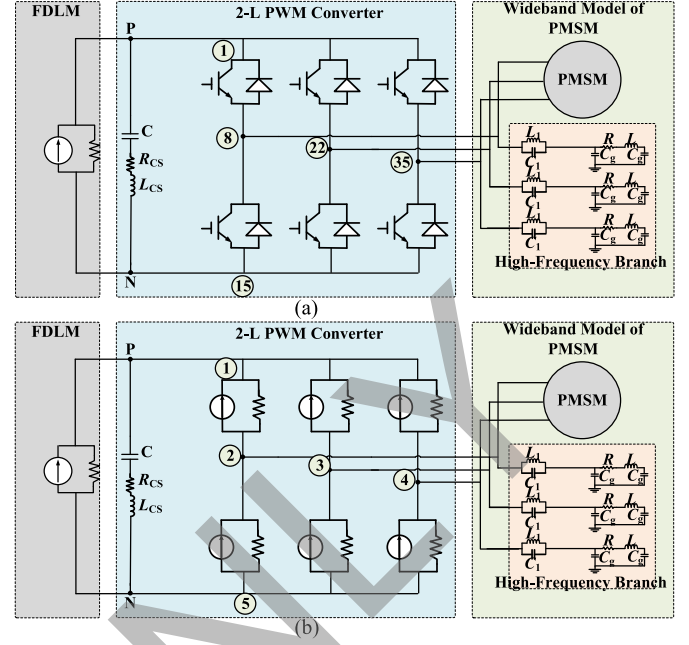


Fig. 6. Circuit partition of 2-L PWM converter. (a) Detailed model. (b) Reduced order model.

All the model parameters can be extracted in Simplorerbased on the datasheet from the manufacturer, as shown in Table IV of Appendix. The IGBT and FWD physical models contain a certain amount of nonlinear components, which brings the main computational burden. The Backward Euler method is used to linearize and discretize the model; thus, an eight-order nodal admittance matrix $\mathbf{Y}_{8 \times 8}^{\text{Node}}$ and eight-dimensional current vector \mathbf{I}_8 are obtained.

B. Universal Parallel Simulation for Different Converter Topology

1) *2-L PWM Converter*: The IGBT modules are assembled by busbars to constitute the structure of the actual converter, which have their own parasitic resistance, inductance, and the stray capacitance. The extraction of these high-frequency-related parameters can be accomplished by ANSYSQ3d. Fig. 6(a) shows the wideband model of a two-level voltage source converter-driven PMSM unit, in which the IGBT modules each have eight nodes with all the parasitic resistance and inductance merged with the terminal stray parameter of the module package. The stray capacitance exists between every two nodes in Fig. 6(b) with the converter, which are not shown in detail in the figure for simplicity.

The circuit has 41 nodes, which will bear an extremely heavy computational burden and take a long time to converge even for a single converter, let alone the whole system, which contains numerous ac-dc transformation units. Thus, each switch module is partitioned from the main circuit and represented by its Norton equivalent unit in every iteration.

To avoid node merging for the short circuit during the Norton equivalent parameter extraction, Thevenin equivalent parameters of each IGBT module are first obtained then transformed into

the corresponding Norton form. The equivalent voltage source of the IGBT is obtained by the solution from:

$$\mathbf{U}_7 = \mathbf{Y}_{7 \times 7}^{-1} \cdot \mathbf{I}_7 \quad (20)$$

where the subscripts mean the dimension of the matrix when the terminal c and e of the physics-based IGBT model is an open circuit. The dimension of the equation is reduced to 7 when node e is treated as the reference. $\mathbf{Y}_{7 \times 7}$ is the reduced-order matrix for the IGBT module with the last row and column of the original admittance matrix deleted, \mathbf{I}_7 is the current vector with the last item deleted accordingly. \mathbf{U}_7 is the nodal voltage, whose first item is the equivalent voltage source of the switch. The equivalent resistance is obtained by the solution of

$$\mathbf{U}_7^{(2)} = \mathbf{Y}_{7 \times 7}^{(2)-1} \cdot \mathbf{I}_7^{(2)} \quad (21)$$

which represents the circuit with terminal c and e of the IGBT connected to an arbitrary dc voltage source V_d . Thus, the first line in $\mathbf{Y}_{7 \times 7}^{(2)}$ is replaced by $[1, 0, 0, 0, 0, 0, 0]$ on the basis of $\mathbf{Y}_{7 \times 7}^{(2)}$, and $\mathbf{I}_7^{(2)}$ is $[V_d, 0, 0, 0, 0, 0, 0]$. With each IGBT represented by its Thevenin equivalent and then transformed to its Norton counterpart, the nodal voltage equation for the converter is simplified to an only five-nodes system, which is obtained by

$$\mathbf{U}_5^{(\text{VSC})} = \mathbf{Y}_{5 \times 5}^{(\text{VSC})-1} \cdot \mathbf{I}_5^{(\text{VSC})}. \quad (22)$$

Then, the nodal voltage $\mathbf{U}_5^{(\text{VSC})}$ of the converter should be assigned to all the inside nodes of every switch:

$$\mathbf{U}_8^{(3)} = \mathbf{Y}_{8 \times 8}^{(3)-1} \cdot \mathbf{I}_8^{(3)} \quad (23)$$

where $\mathbf{U}_8^{(3)}$ is the updated voltage of all the eight nodes for each module, $\mathbf{Y}_{8 \times 8}^{(3)}$ is the matrix obtained from $\mathbf{Y}_{8 \times 8}$ with the first and last row substituted by $[1, 0, 0, 0, 0, 0, 0, 0]$ and $[0, 0, 0, 0, 0, 0, 0, 1]$. $\mathbf{I}_8^{(3)}$ is the current vector with the first and last item substituted by the corresponding nodal voltage in $\mathbf{U}_5^{(\text{VSC})}$. Therefore, the voltage values of all the nodes are obtained and can be sent to next iteration. This method can also be generalized to the 3-L NPC topology.

2) *Modular Multilevel Converter*: MMC is already widely used in today's HVdc projects and propulsion system for the railway, ship, and foreseeable extension on the MEA. Different from the 2-L PWM and 3-L NPC converter, in which the commutation unit is located in both arms of the same phase inside the converter, the commutation of MMC happens within each submodule.

The distribution of the stray parameter inside an MMC is quite complicated, which not only includes the parasitics inductance and resistance of the bond wires and the connectors of the semiconductor module and busbar, but also the complex stray capacitance network shown in Fig. 7(a).

Fortunately, the stray capacitance at the terminals of the SMs can be used as the medium to decouple them from the main circuit [22]. The capacitance is regarded as a two-port device, and the system can, thus, be decoupled with both sides represented by its Norton equivalent form, as shown in Fig. 7(b), so that the SMs and the arm bridge can be solved as two separated circuits, while the history value-dependent current source maintain the information exchange between the decoupled components.

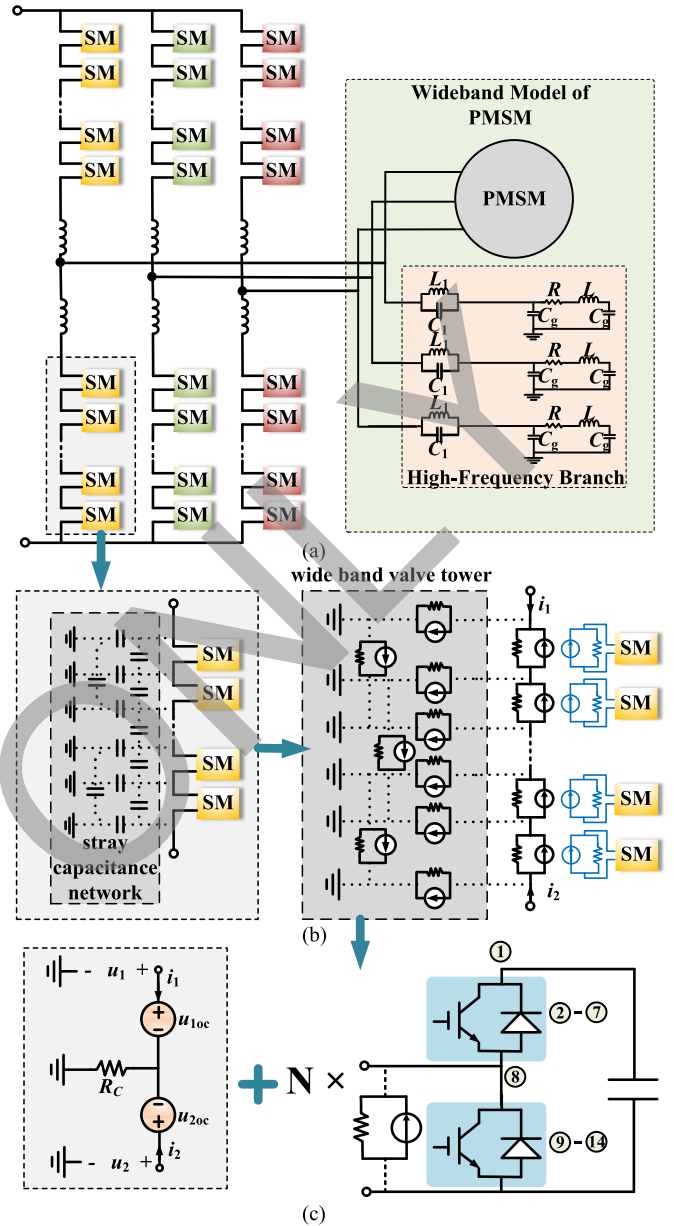


Fig. 7. Circuit partitioning of MMC. (a) Wideband model of MMC. (b) TLM link model of the stray capacitance. (c) SM decoupling.

With the capacitance represented by their discretized circuit, the wideband model of the converter arm constitute a two-port network with an internal independent current source, which can be further simplified into the form shown in Fig. 7(c). The process for the transformation can achieve a highly parallel implementation.

IV. PARALLEL IMPLEMENTATION OF WIDEBAND MEA MICROGRID SYSTEM ON GPU

A. Hardware Implementation

In order to support the application of CPU + GPU heterogeneous system architecture to execute program, NVIDIA developed a universal programming interface for GPU, namely,



Fig. 8. Volta architecture of NVIDIA Tesla V100 GPU. (a) Streaming multiprocessor architecture. (b) Overall architecture.

Compute Unified Device Architecture (CUDA), which is integrated with C or C++ language to realize parallel program development. A CUDA program contains host code running on CPU and device code running on GPU, which is also called a kernel function. CUDA manages threads in terms of thread wraps, each of which contains 32 threads with its own instruction address counter and registration status. All threads in the wrap execute the same instruction at the same time, which is also called single instruction multithreading architecture.

As for hardware, GPU hardware architecture takes the streaming multiprocessor as an extensible unit and achieves parallelism by copying it to form an array building block. Each streaming multiprocessor in GPU can support hundreds of concurrent threads. The kernel functions of parallel programs are scheduled according to the availability of streaming multiprocessor resources and are allocated to the available streaming multiprocessors for parallel execution.

The program is executed on the NVIDIA Tesla V100 GPU with Volta architecture, which contains six GPU processing clusters (GPC). Each cluster contains seven texture processing clusters, which contains two streaming multiprocessors. As shown in Fig. 8(a), each streaming multiprocessor contains 64 32-bit floating-point arithmetic cores, 64 32-bit integer

arithmetic cores, 32 64-bit floating-point arithmetic cores, eight tensor cores, and four texture units. The whole GPU contains 8 512-bit memory controllers (4396 bits in total). Therefore, the complete V100 GPU with 84 streaming multiprocessors has a total of 5376 fp32 cores, 5376 int32 cores, 2688 fp64 cores, 672 tensor cores, and 336 texture units. Each HBM2 DRAM stack is controlled by a pair of memory controllers, as shown in Fig. 8(b).

B. Details of Kernels and Threads

As shown in Fig. 9, all the aforementioned algorithms are programmed on the CUDA C platform with the corresponding function module designed as a specific kernel. All the kernels are executed one after another, then update and transfer the variable through the global memory. Each kernel evokes a series of threads, in which the functions are operated in the single instruction multiple thread (SIMT) parallel manner. The amount of the threads depends on the number of the module in the system accordingly. The kernel₁ and kernel₂ are the wideband models of the synchronous generator and PMSM [24], which utilize the ac terminal voltage as the input and produce the ac current as the feedback to the system. According to the collection of the motor speed and system voltage, the trigger signal of the converter is generated in kernel₃.

The kernel₄ and kernel₅ need to be solved iteratively due to the semiconductor power device model. In kernel₄, the wideband model of the autotransformer [25] is integrated at the ac terminal of the rectifier along with the split FDLM section.

The content of kernel₅ depends on which kind of converter topology is installed in the system. If a 2-L PWM converter is selected, four kernels of the subgeneration are included corresponding to the solving process in (24)–(27). As for the MMC, the iterative calculation for the output of all the SMs is conducted in the first subkernel, and then the second one collects them to form the node equation for the wideband model for the whole converter. Then, the historical value of stray capacitance is updated. Finally, the FDLM kernel gathers all the history value-dependent current and has its terminals interacted.

C. Simulation Results

The comparative simulation is conducted on Simplorer and carried out on a PC with Intel Core i7-6700 CPU, 3.6 GHz clock frequency, and 8 GB RAM. The time-step is set to 10 ns, and the total simulation period is 2 s. It takes the ANSYS Simplorer simulation 4.12 and 36.36 h for the system with 2-L converter and MMC, respectively, while only 1.45 and 4.01 h for the parallel algorithm on GPU, and the corresponding speed-up is about 2.84 and 9.07 times. Noted that the simulation time will not increase significantly with the expansion of the system scale or the increase of the MMC level due to the massive parallelism.

Figs. 10 and 11 show the time-domain result of both the proposed method and the simulation on the commercial simulation platform. The ac voltage in both the cases for the 2-L

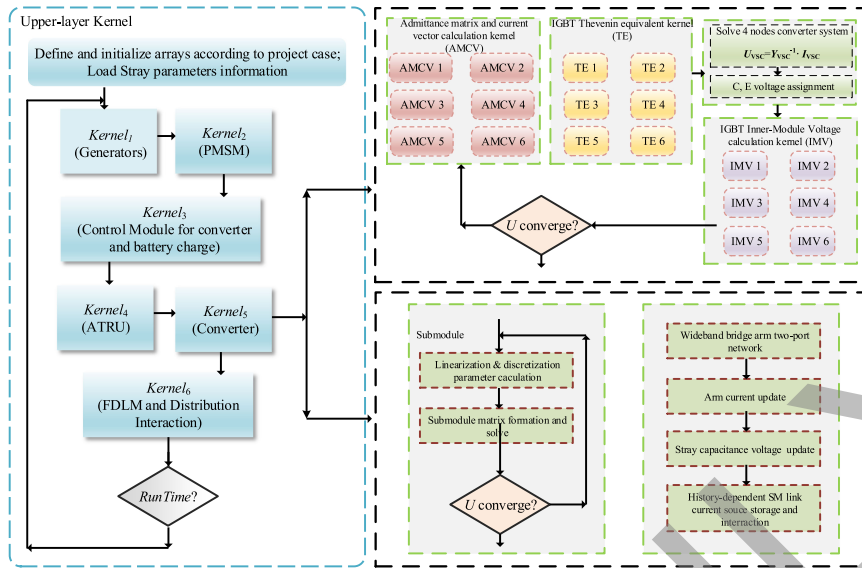


Fig. 9. Flowchart of the parallel simulation for the MEA microgrid.

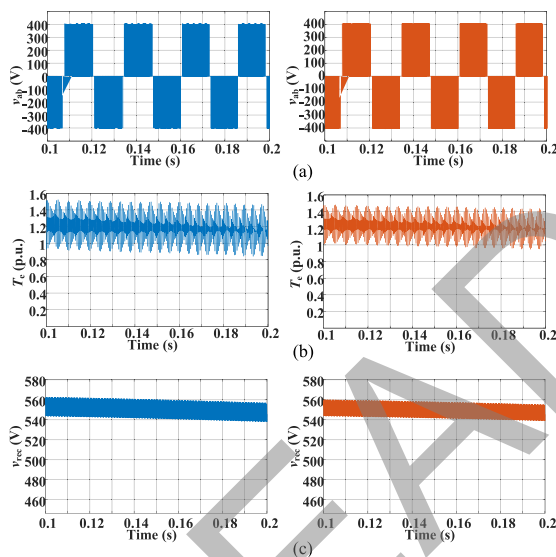


Fig. 10. Comparison between GPU-based simulation and ANSYS Simplorer in time domain. (a) Line-to-line voltage of PMSM for 2-L converter. (b) Electromagnetic torque of PMSM. (c) 12 pulse voltage of ATRU.

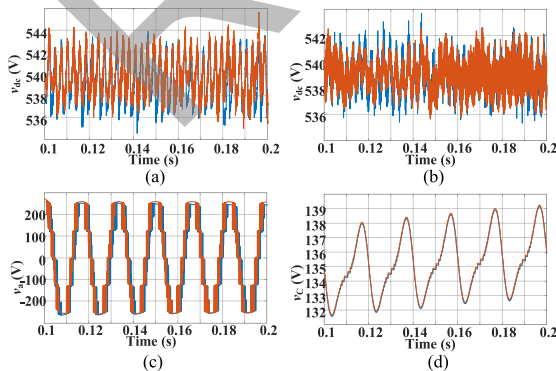


Fig. 11. Comparison between GPU-based simulation and ANSYS Simplorer in time domain. (a) DC busbar voltage for MMC. (b) DC busbar voltage for 2-L converter. (c) Line-to-ground voltage of PMSM for MMC. (d) SM capacitor voltage for MMC.

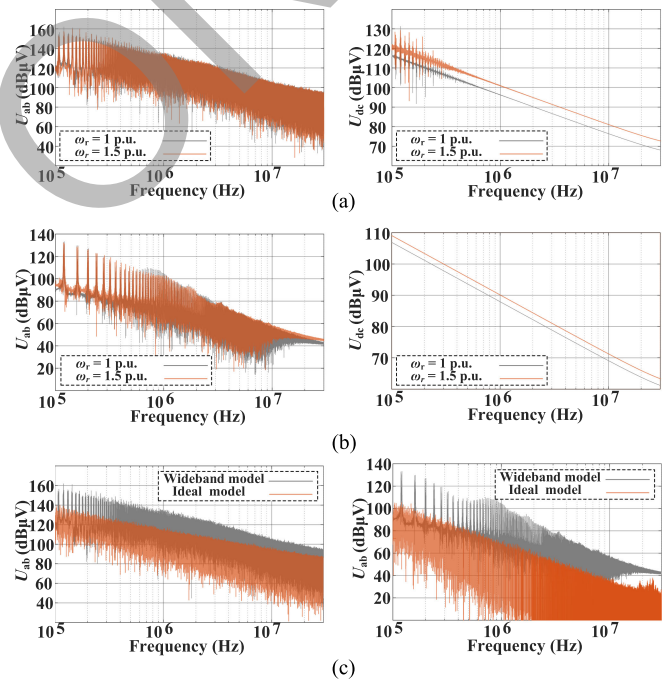


Fig. 12. Frequency-domain results. (a) Impact of PMSM speed on conducted EMI of ac and dc side for 2-L converter. (b) Impact of PMSM speed on conducted EMI of ac and dc side for MMC. (c) Impact of wideband characteristics.

converter and MMC are all nicely fitted with the result from Simplorer. As regards to the dc voltage of the busbar, there is slight deviation. However, the fluctuation is basically in the same range with the same peak and valley times. The waveform of the capacitor voltage proves that the converter achieves a good voltage balance.

Fig. 12 shows the result under different PMSM speed in the frequency domain. It can be concluded that the promotion of rotate load will lead to a significant increase in the dc voltage for both converters, while the influence on ac voltage is negligible.

Thus, more attention should be put on the dc side with careful design for the filter if higher motor speed is to be achieved. Fig. 12(c) shows the application of ideal switch model will lead to serious underestimation and miscalculation of the EMI level.

It should be highlighted that the application of MMC will obtain a great suppression of the EMI at both the ac and dc sides, especially for the dc voltage. Thus, if the weight increases from the numerous semiconductor devices inside the MMC can be offset by removing of the filter, MMC will undoubtedly be an excellent option for the future MEA microgrid.

V. CONCLUSION

This article has demonstrated a universal wideband time-domain simulation method for MEA with the physics-based model of the IGBT modules and the high-frequency branches for other components included. The resultant computational burden was alleviated via the circuit partitioning based on the FDLM of the cable, which can split the whole microgrid system into several subcircuits with a significantly reduced scale of matrix solution and the possibility to realize parallel processing. Considering the nonlinear behavior of the semiconductor devices and its unavoidable iteration, to achieve further simulation acceleration, fine-grained partition for the converter of various topology has been proposed. For the 2-L PWM based and 3-L NPC converters, the Norton equivalent parameter of all the module units is extracted simultaneously during each iteration process. For an MMC with significantly more switches, the SMs are decoupled from the bridge arm based on the TLM link model of the stray capacitance connected at the terminals. This partitioning scheme can greatly increase the parallelism level of the model. The effectiveness and accuracy of the proposed method are verified by comparison with the simulation results of Simplorer for the study case of the Boeing 787 aircraft microgrid system. The results of the frequency domain analysis show that the application of MMC will help to suppress the EMI.

APPENDIX

TABLE I
MODEL PARAMETERS OF DC FDLM

$\alpha_{Y_c} = 1, 1, 1, 1, 1, 0.9997, 0.9950,$
$\lambda_{Y_c} = 5e-9, 5e-9, 5e-9, 5e-9, 5e-9, 4.9992e-9, 4.9875e-9,$
$\mu_{Y_c} = 5e-9, 5e-9, 5e-9, 5e-9, 5e-9, 4.9992e-9, 4.9875e-9.$

TABLE II
MODEL PARAMETERS OF AC FDLM

$\alpha_{Y_c} = 1, 1, 1, 1, 1, 0.9996,$
$\lambda_{Y_c} = 5e-9, 5e-9, 5e-9, 5e-9, 5e-9, 4.9989e-9,$
$\mu_{Y_c} = 5e-9, 5e-9, 5e-9, 5e-9, 5e-9, 4.9989e-9.$

TABLE III
MODEL PARAMETERS OF PMSM

$S_N = 0.06 \text{ MVA}, U_N = 300 \text{ V}, r_s = 0.0021, X_s = 0.064,$
$X_d = 0.689, X_q = 0.689, r_{kd} = 0.055, X_{kd} = 0.62,$
$r_{kq} = 0.183, X_{kq} = 1.175, R = 9.95\Omega, L = 46.15\mu\text{H},$
$C_g = 12.01\text{nF}.$

TABLE IV
MODEL PARAMETERS OF INFINEON FF600R07ME4

$V_P = 1.59, K = 3.68, KLM = 0.001, A_{FET} = 1.21, M_{FET} = 0.57,$
$N_{FET} = 1.58, bn = 15, M_{bjt} = 0.93, I_{satbjt} = 2.56^{-8}, R_{sh} = 10^6,$
$M_{fwd} = 1.06, I_{satfwd} = 1e-6, R_b = 0.0015, C_{0gs} = 5.43^{-8},$
$\alpha_{ge} = 0.8, \delta_{ge} = 0.5, C_{0eg} = 4.97 \times 10^{-12}, V_{egdiff,off} = 2,$
$\alpha_{egoff} = 0.5, \alpha_{egon} = 0.5, \beta_{egoff} = 1.01, \beta_{egon} = 2.95, \delta_{egoff} = 0.41,$
$\delta_{egon} = 0.06, C_{0ec} = 7.39^{-9}, V_{ecdiff} = 0.7, \alpha_{ec} = 0.5, \beta_{ec} = 1.01,$
$\delta_{ec} = 0.1, \tau_{eb} = 1.06 \times 10^{-7}, \tau_s = 9.35 \times 10^{-8}, \tau_{fwd} = 2.25 \times 10^{-9},$
$\tau_{tail} = 3.68 \times 10^{-7}, \delta_{tail} = 0.34, R_{1fwd} = 0.75, R_{2fwd} = 0.7,$
$SF1_{fwd} = 1.5, SF2_{fwd} = 3, L_C = 35.9 \times 10^{-9}, R_C = 5.3e^{-6},$
$L_E = 23.2 \times 10^{-9}, R_E = 5.3 \times 10^{-6}, L_G = 26.1 \times 10^{-9}, R_G = 0.2,$
$R_{g,ext} = 10, T_n = 3.75 \times 10^{-14}, K_{gshif} = 3.75, V_{egdiff,on} = 1,$
$R3_{fwd} = 0.2.$

REFERENCES

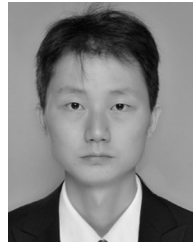
- [1] P. Wheeler and S. Bozhko, "The more electric aircraft: Technology and challenges," *IEEE Electr. Mag.*, vol. 2, no. 4, pp. 6–12, Dec. 2014.
- [2] V. Madonna, P. Giangrande, and M. Galea, "Electrical power generation in aircraft: Review, challenges, and opportunities," *IEEE Trans. Transp. Electr.*, vol. 4, no. 3, pp. 646–659, Sep. 2018.
- [3] R. D. Leach and M. B. Alexander, "Electronic systems failures and anomalies attributed to electromagnetic interference," NASA Reference Publication, Washington, DC, USA, vol. 1374, Jul. 1995.
- [4] N. L. Armstrong and Y. M. M. Antar, "Investigation of the electromagnetic interference threat posed by a wireless network inside a passenger aircraft," *IEEE Trans. Electromagn. Compat.*, vol. 50, no. 2, pp. 277–284, May 2008.
- [5] A. Charalambous, X. Yuan, and N. McNeill, "High-frequency EMI attenuation at source with the auxiliary commutated pole inverter," *IEEE Trans. Power. Electron.*, vol. 33, no. 7, pp. 5660–5676, Jul. 2018.
- [6] Z. Huang and V. Dinavahi, "An efficient hierarchical zonal method for large-scale circuit simulation and its real-time application on more electric aircraft microgrid," *IEEE Trans. Ind. Electron.*, vol. 66, no. 7, pp. 1491–1498, Nov. 2018.
- [7] Z. Huang, C. Tang, and V. Dinavahi, "Unified solver based real-time multi-domain simulation of aircraft electro-mechanical-actuator," *IEEE Trans. Power. Electron.*, vol. 34, no. 4, pp. 1491–1498, Nov. 2019.
- [8] N. Lin and V. Dinavahi, "Behavioral device-level modeling of modular multilevel converters in real time for variable-speed drive applications," *IEEE J. Emerg. Sel. Topics Power Electron.*, vol. 5, no. 3, pp. 1177–1191, Sep. 2017.
- [9] N. Lin and V. Dinavahi, "Exact nonlinear micro-modeling for fine-grained parallel EMT simulation of MTDC grid interaction with wind farm," *IEEE Trans. Ind. Electron.*, vol. 33, no. 6, pp. 4660–4678, Jun. 2018.
- [10] F. Costa and D. Magnon, "Graphical analysis of the spectra of EMI sources in power electronics," *IEEE Trans. Power. Electron.*, vol. 20, no. 6, pp. 1491–1498, Nov. 2005.
- [11] J. Meng, W. Ma, Q. Pan, L. Zhang, and Z. Zhao, "Multiple slope switching waveform approximation to improve conducted EMI spectral analysis of power converters," *IEEE Trans. Electromagn. Compat.*, vol. 48, no. 4, pp. 742–751, Nov. 2006.
- [12] V. S. Nguyen, P. Lefranc, and J. C. Crebier, "Gate driver supply architectures for common mode conducted EMI reduction in series connection of multiple power devices," *IEEE Trans. Power. Electron.*, vol. 33, no. 12, pp. 12265–10276, Sep. 2018.
- [13] Z. Yu *et al.*, "Simulation analysis on conducted EMI caused by valves in $\pm 800 \text{ kV}$ UHVDC converter station," *IEEE Trans. Electromagn. Compat.*, vol. 51, no. 2, pp. 236–244, May 2009.

- [14] F. Costa, C. Vollaïre, and R. Meuret, "Modeling of conducted common mode perturbations in variable-speed drive systems," *IEEE Trans. Electromagn. Compat.*, vol. 47, no. 4, pp. 1012–1021, Nov. 2005.
- [15] A. Nejadpak and O. Mohammed, "Physics-based modeling of power converters from finite element electromagnetic field computations," *IEEE Trans. Magn.*, vol. 49, no. 1, pp. 567–576, Jan. 2013.
- [16] D. Jiang, R. Lai, F. Wang, F. Luo, S. Wang, and D. Boroyevich, "Study of conducted EMI reduction for three-phase active front-end rectifier," *IEEE Trans. Power Electron.*, vol. 26, no. 12, pp. 3823–3831, Jun. 2011.
- [17] Y. Xiang, X. Pei, W. Zhou, Y. Kang, and H. Wang, "A fast and precise method for modeling EMI source in two-level three-phase converter," *IEEE Trans. Power Electron.*, vol. 34, no. 11, pp. 10650–10664, Sep. 2019.
- [18] D. Labrousse, B. Revol, C. Gautier, and F. Costa, "Fast reconstitution method (FRM) to compute the broadband spectrum of common mode conducted disturbances," *IEEE Trans. Electromagn. Compat.*, vol. 55, no. 2, pp. 248–256, Jun. 2016.
- [19] G. Buticchi, S. Bozhko, M. Liserre, P. Wheeler, and K. Al-Haddad, "On-board microgrids for the more electric aircraft? Technology review," *IEEE Trans. Ind. Electron.*, vol. 66, no. 7, pp. 5588–5599, Jul. 2019.
- [20] B. Sarlioglu and C. T. Morris, "More electric aircraft: Review, challenges, and opportunities for commercial transport aircraft," *IEEE Trans. Transp. Electric.*, vol. 1, no. 1, pp. 54–64, Jun. 2015.
- [21] T. Duan and V. Dinavahi, "Adaptive time-stepping universal line and machine models for real-time and faster-than-real-time hardware emulation," *IEEE Trans. Ind. Electron.*, vol. 67, no. 8, pp. 6173–6182, Aug. 2020.
- [22] S. Y. R. Hui and K. K. Fung, "Fast decoupled simulation of large power electronic systems using new two-port companion link models," *IEEE Trans. Power Electron.*, vol. 12, no. 3, pp. 462–473, May 1997.
- [23] ANSYS, Inc., *Simplorer Components: Basic Elements*, Canonsburg, PA, USA, Jul. 2018.
- [24] O. Mohammed, S. Ganu, N. Abed, S. Liu, and Z. Liu, "High frequency PM synchronous motor model determined by FE analysis," *IEEE Trans. Magn.*, vol. 42, no. 4, pp. 1291–1294, Apr. 2006.
- [25] X. Perpinya, "Infrastructure design, signaling and security in railway" IntechOpen, London, U.K., Apr. 2012.



Ruimin Zhu (Student Member, IEEE) received the B.Eng. degree in electrical engineering from North China Electric Power University, Baoding, China, in 2012. He is currently working toward the Ph.D. degree with North China Electric Power University, Beijing, China. In 2018 and 2019, he was a Joint Ph.D. Student with RTXLAB, University of Alberta, Edmonton, AB, Canada.

His research interests include EMI analysis of power systems, power electronics, device-level modeling, and parallel simulation.



Zhen Huang (Student Member, IEEE) received the B.Eng. degree in electrical engineering from Xi'an Jiaotong University, Xi'an, China, in 2012 and the M.Eng. degree in electrical engineering from Tsinghua University, Beijing, China, in 2015. He is currently working toward the Ph.D. degree with the Department of Electrical and Computer Engineering, University of Alberta, Edmonton, AB, Canada.

He also has two years work experience in power electronic industry. His research interests include high-performance simulation and control of power electronics.



Venkata Dinavahi (Fellow, IEEE) received the B.Eng. degree in electrical engineering from the Visveswaraya National Institute of Technology (VNIT), Nagpur, India, in 1993, the M.Tech. degree in electrical engineering from the Indian Institute of Technology (IIT) Kanpur, Kanpur, India, in 1996, and the Ph.D. degree in electrical and computer engineering from the University of Toronto, Toronto, ON, Canada, in 2000.

He is currently a Professor with the Department of Electrical and Computer engineering, University of Alberta, Edmonton, AB, Canada. His research interests include real-time simulation of power systems and power electronic systems, electromagnetic transients, device-level modeling, large-scale systems, and parallel and distributed computing.